Planar Transformer with Asymmetric Integrated Leakage Inductance Using Horizontal Air Gap

Michael D'Antonio, *Student Member, IEEE*, Shiladri Chakraborty, *Member, IEEE*, and Alireza Khaligh, *Senior Member, IEEE*

Abstract—This manuscript presents a novel planar-based transformer winding and core structure with controllable leakage inductance generation for integrated magnetics applications. As a result of limitations in integrated magnetics from the literature, a new approach is proposed utilizing semi-interleaved windings and controllable leakage via a leakage flux core leg featuring a horizontal air gap. The proposed transformer design is analyzed via detailed reluctance modeling to determine closed-form equations for the magnetizing and asymmetrically distributed leakage inductances. Next, a genetic-algorithm-based multi-objective design optimization problem is developed, seeking to minimize the core and winding losses of the proposed transformer subject to a set of parametric and geometric constraints in a DC-AC dual-active-bridge topology for microinverter applications. The optimization was extended to include other integrated magnetics structures from the literature, where it is determined that the proposed transformer is superior from the perspectives of efficiency, footprint area, and parasitic capacitance. Based on the results of the optimization analysis, two designs with theoretical transformer CEC efficiency drops (i.e. CEC efficiency reduction specifically due to the transformer loss mechanisms) of 1.19% and 0.83% were fabricated and evaluated for electrical and thermal performance in the proposed 40 V, 400 W microinverter.

I. Introduction

High-frequency transformers are at the heart of many widely used isolated power converter topologies like flyback, phase-shifted-full-bridge (PSFB), resonant (LLC, CLLC), and dual-active-bridge (DAB), among others [1]. In flyback and PSFB-based topologies, the leakage inductance of the transformer is an undesirable parasitic element, which leads to voltage spikes across switches and is thus intended to be kept as low as possible in a good design. On the contrary, resonant and DAB-based topologies include an impedance network between the primary and secondary side of the transformer, consisting of series and parallel inductances. The series inductor acts as an energy storage and delivery element and is hence not intended to be minimal. Rather, its value should be high enough to

The authors are with the Department of Electrical and Computer Engineering, Maryland Power Electronics Laboratory, Institute for Systems Research, University of Maryland, College Park, MD - 20742, U.S.A (e-mail: michaeld@umd.edu, shiladri@umd.edu, khaligh@umd.edu.)

Color versions of one or more of the figures in this paper are available online at http://ieeexplore.ieee.org.
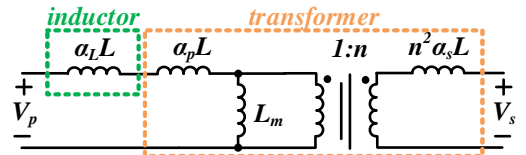

Fig. 1. General magnetics implementation consisting of an inductor and transformer. In non-integrated magnetics applications, the series inductor (with α_L=1) and ideally low leakage transformer (where $\alpha_p \approx \alpha_s \approx 0$) are implemented with independent core and winding sets. In integrated magnetics applications, the series inductor can be eliminated (with $\alpha_L = 0$) as the desired inductance is integrated into the transformer's leakage inductance. For the integrated case, the inductor's distribution could be arbitrarily set, where $\alpha_p + \alpha_s \approx 1$ when L_m is sufficiently larger than L.

satisfy power-flow, voltage-gain, and zero-voltage-switching (ZVS) requirements of the circuit.

Traditionally the inductance network would be realized by a discrete series inductor and a near-ideal transformer with low leakage inductance, represented in Fig. 1 when $\alpha_L \approx 1$ and $\alpha_p \approx \alpha_s \approx 0$. More recently, following the trend to design converters with low cost, low loss, and high power density, integration of the series inductor and transformer has been proposed, where the series inductance is realized by the transformer's leakage inductance [2]. To further improve the performance of the integrated structure, an increase in circuit switching frequency has been coupled with the utilization of planar cores with low profile height [2]. The integrated transformer case is also shown in Fig. 1 where $\alpha_L \approx 0$ and $\{\alpha_p, \alpha_s\} \neq 0$, and hence the inductance distribution in the transformer could be arbitrarily designed.

Previous literature has investigated different ways to controllably achieve desired values of leakage inductance and magnetizing inductance into a single transformer structure [2]- [16]. In general, the techniques for leakage integration involve manipulation of the transformer core structure [4]-[6], insertion of additional magnetic materials into the core structure [7]- [13], or manipulation of the winding structure [14]- [16]. The approach in [4] considers the use of vertically stacked transformer and inductor cores, exhibiting limitations in complex transformer core implementation and multiple winding PCBs. An improved planar-based matrix transformer implementation is considered in [5]- [6], where the magnetics core structure includes designated legs and flux paths for a series inductance and ideal transformer.

In [7]- [9], the primary- and secondary-side windings are both wound around the transformer core center leg, and controllable leakage inductance is realized by placing an intentional air-gap between the primary- and secondary-side wind-
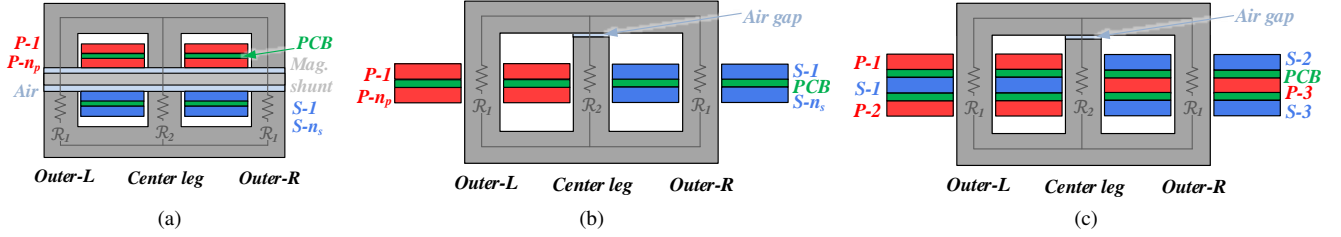
Fig. 2. Integrated transformer implementations from the literature with controllable leakage generated through, (a) air-gap or magnetic shunt material between the primary- and secondary-side windings, (b) relative reluctance of the outer and center legs with primary- and secondary-side windings wound around separate core outer legs (shell transformer), and (c) relative reluctance of the outer and center legs with asymmetrically distributed primary- and secondary-side windings (ACL transformer). Terms n_p and n_s denote an arbitrary number of winding layers used for the primary- and secondary-side windings, where each winding layer is comprised of m_p and m_s number of turns.

ings, as shown in Fig. 2(a). Importantly, this winding structure requires separate PCBs for the two windings, which may compromise cost and manufacturability of the transformer. Furthermore, the maximum achievable leakage inductance is limited by the height of the air-gap between the windings. An alternative approach for this winding configuration with axial air gap separation between the primary- and secondary-side windings is presented in [10], where limitations exist in the usage of non-planar windings and maximum limits on the leakage inductance. To circumvent the limitation in maximum leakage inductance in air-gap implementations, [11]-[13] propose the use of a magnetic shunt (i.e. an additional core material with larger than unity permeability) located in the gap between the windings, also shown in Fig. 2(a). However, the magnetic shunt increases the transformer core complexity and assembly cost, incurs additional core loss in the transformer, and has temperature-dependent permeability leading to non-stable leakage inductance [9]. Furthermore, [7]- [12] do not achieve good winding interleaving, which will increase conduction-related losses due to the large DC-to-AC resistance ratio. A further extension in [13] proposes to include winding sets both on the transformer center leg as well as the magnetic shunt, which will have difficulties in manufacturability and conduction loss.

With regards to winding manipulation, [14] proposed to wind the primary- and secondary-side windings around the outer-left and outer-right legs of the transformer, shown in Fig. 2(b). In this design, hereby termed the 'Shell' transformer, controllable leakage inductance is generated through proper design of the core center leg. However, while the windings could be implemented on a simple two- or four-layer PCB with minimal complexity, the transformer has a large footprint area, as the windings fully extend outside the transformer core. Furthermore, the AC resistance in this design is high, as the windings are not interleaved.

To address the issue of high AC resistance in the shell transformer, [15] proposes to wind the primary- and secondary-side windings asymmetrically (i.e. placing a different number of primary- and secondary-side turns) around the outer legs of the transformer core as shown in Fig. 2(c). In light of the winding structure, this transformer is henceforth deemed the asymmetrically-wound controllable leakage transformer (ACL). By asymmetrically distributing the windings, controllable leakage inductance can be generated by tuning the core

reluctances, and winding interleaving is achieved. However, the winding structure is complex, as windings need to be routed around both the left and right core legs. Furthermore, for the advantages in AC resistance from winding interleaving, the structure has high overlap area between the primary- and secondary-side windings, which could generate undesirable amounts of inter-winding capacitance. A similar approach is also proposed in [16], however the windings are not interleaved as effectively as in [15], and hence will likely result in increased AC resistance.

In all of the current state-of-the-art, there are limitations associated with subsidiary effects of the leakage inductance integration. Generally these limitations include: complexity in the core structure [4]- [5], [11]- [13], complexity in winding structure [7]- [13], [15]- [16], and high AC resistances due to winding structure [7]- [14]. As such the principal contribution of this manuscript is to develop a transformer core plus winding structure that, 1) is capable of realizing controllable leakage inductance, 2) utilizes a simple core structure and winding layout that can be realized on a low-cost four layer PCB, 3) achieves at least partial winding interleaving for low DC-to-AC resistance ratio, and 4) has low winding overlap area such that the parasitic capacitances do not degrade circuit performance. Furthermore, the second key contribution of the manuscript is to develop a transformer geometry optimization procedure, which will be used to design the proposed transformer in a single-stage DAB-based 400 W microinverter application and enable design comparison to other transformer structures from the literature.

The manuscript is organized as follows: Section II presents reluctance modeling for the proposed transformer; the target topological application is developed in Section III, alongside the associated loss modeling; a multi-objective design optimization is presented in Section IV; finally, Section V presents experimental results.

II. ELECTRICAL MODELING OF PROPOSED TRANSFORMER

A. Overview of the Proposed Design

A cross-section view of the proposed transformer design is shown in Fig. 3, including the core, the core's equivalent reluctance model, and the transformer windings [1]. The core can be realized through the use of an E-core, plus two I-core segments separated by an air gap. In light of the construction, the proposed implementation is henceforth referred to as the
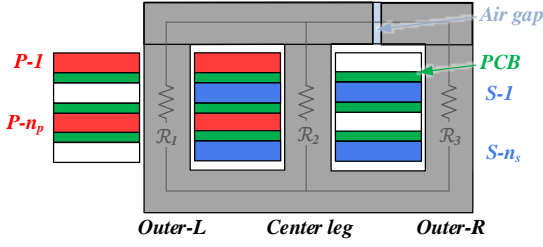
Fig. 3. Core and winding diagram of the proposed EII transformer. Within the core is the equivalent reluctance network, realized by a single equivalent reluctance for each core leg. Each winding layer may be comprised of an arbitrary number of turns. White portions in the winding structure indicate the absence of turns on the respective PCB layer.

'EII' transformer. As can be observed, the terminal windings are wound around the left leg and the center leg, achieving partial interleaving in the left core window. The mutual flux path is completed between the outer left leg and the center leg, while the leakage flux path is completely between the winding legs and the outer right leg. Due to the fact that the leakage flux path is completed through the outer right leg, there is freedom to place an air gap anywhere along the core leg. As such, the air gap is shown to be placed along the top-section of the core (deemed a horizontal air-gap) to reduce the magnitude of the perpendicular component of the H-field at the winding, and improve the H-field symmetry along the cross-section of the windings [17]. As a result, the winding DC-to-AC resistance ratio is reduced as compared to placement of the air gap along the vertical section of the core.

B. Reluctance Modeling

The detailed reluctance model of the core is presented in Fig. 4. Due to the fact that the mutual flux path is un-gapped in the proposed implementation (where otherwise the air-gap is a dominant reluctance component compared to the core reluctances), consideration of separate reluctances for the corners and straight core segments is critical, originally motivated and modeled in [18]. The considered lengths and areas of each reluctance segment is shown in Table I, and the reluctances can be calculated via,

$$\mathcal{R}_x = \frac{l_x}{\mu_{r,x}\mu_0 A_x} \quad (1)$$

where l_x is the length of the reluctance segment, A_x is the effective cross-section area of the reluctance segment, and $\mu_{r,x}$ is the relative permeability of the core segment. The air-gap reluctance is important to model as accurately as possible, as it is the largest reluctance component in the network. Consideration of 3-D fringing effects can easily be calculated via the formulation derived in [18], where in this case a type-I air-gap is utilized.

Conversion of the detailed reluctance network in Fig. 4(a) to the equivalent network in Fig. 4(b) can be facilitated by,

$$\mathcal{R}_1 = \mathcal{R}_{side} + 2\mathcal{R}_{c,1} + 2\mathcal{R}_{c,2} + \mathcal{R}_{top} + \mathcal{R}_{bot} \quad (2)$$

$$\mathcal{R}_2 = \mathcal{R}_{side} \quad (3)$$

$$\mathcal{R}_3 = \mathcal{R}_{gap} + \mathcal{R}_{lk} + 2\mathcal{R}_{c,2} + 2\mathcal{R}_{c,3} + \mathcal{R}'_{top} + \mathcal{R}_{bot} \quad (4)$$
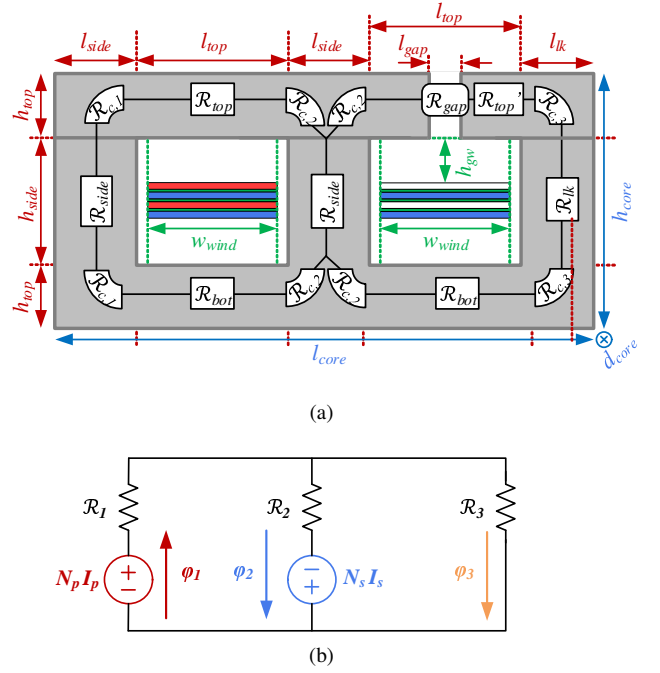

(a)

(b)

Fig. 4. Proposed transformer (a) detailed core reluctance modeling, and (b) equivalent reluctance network modeling. In (a), inner core dimensions are labeled in red, while the external core dimensions are labeled in blue. Additional dimensions related to the winding structure are identified in green. The primary-side windings extending outside of the core footprint on the left have not been shown for simplicity.

TABLE I. LENGTHS AND AREAS FOR EACH RELUCTANCE IN FIG. 4(a).

Reluctance (x)	Length	Area
Side (side)	h_{side}	$l_{side}d_{core}$
Corner 1 (c1)	$\pi(h_{top}+l_{side})/8$	$d_{core}(h_{top}+l_{side})/2$
Top / bot (top / bot)	l_{top}	$h_{top}d_{core}$
Corner 2 (c2)	$\pi(h_{top}+l_{side}/2)/8$	$d_{core}(h_{top}+l_{side}/2)/2$
Top' (top')	$l_{top}-l_{gap}$	$h_{top}d_{core}$
Gap (gap)	l_{gap}	$h_{top}d_{core}$
Leak (lk)	h_{side}	$l_{lk}d_{core}$
Corner 3 (c3)	$\pi(h_{top}+l_{lk})/8$	$d_{core}(h_{top}+l_{lk})/2$

From the equivalent circuit, equations for the flux in each of the three core legs can be derived as,

$$\phi_1 = \frac{N_pI_p(\mathcal{R}_2+\mathcal{R}_3)-N_sI_s\mathcal{R}_3}{\mathcal{R}_T} \quad (5)$$

$$\phi_2 = \frac{-N_pI_p\mathcal{R}_3+N_sI_s(\mathcal{R}_1+\mathcal{R}_3)}{\mathcal{R}_T} \quad (6)$$

$$\phi_3 = \frac{N_pI_p\mathcal{R}_2+N_sI_s\mathcal{R}_1}{\mathcal{R}_T}, \quad (7)$$

where $\mathcal{R}_T = \mathcal{R}_1\mathcal{R}_2 + \mathcal{R}_1\mathcal{R}_3 + \mathcal{R}_2\mathcal{R}_3$, $N_p = n_pm_p$ and $N_s = n_sm_s$ are the total number of primary- and secondary-side turns (n_p and n_s are the number of winding layers on the primary- and secondary-sides, m_p and m_s are the number of primary- and secondary-side turns on each winding layer), and I_p and I_s are the terminal currents of the primary- and secondary-side. Using the flux expressions in each of the three core legs, the self- and mutual-inductances of each coil can be derived as,

$$L_{s,p} = \frac{N_p \phi_1|_{I_s=0}}{I_p} = \frac{N_p^2 (\mathcal{R}_2 + \mathcal{R}_3)}{\mathcal{R}_T} \qquad (8)$$

$$L_{s,s} = \frac{N_s \phi_2|_{I_p=0}}{I_s} = \frac{N_s^2 (\mathcal{R}_1 + \mathcal{R}_3)}{\mathcal{R}_T} \qquad (9)$$

$$M = \frac{N_s \phi_2|_{I_s=0}}{I_p} = \frac{N_p N_s \mathcal{R}_3}{\mathcal{R}_T} \qquad (10)$$

Based on these equations, the magnetizing and leakage inductance in the transformer T-model of Fig. 1 can be determined through subtraction of the self and mutual terms and reflection by the transformer turns ratio [3],

$$L_{lk,p} = L_{s,p} - M/N = \frac{N_p^2 \mathcal{R}_2}{\mathcal{R}_T} \qquad (11)$$

$$L_{lk,s} = L_{s,s} - M \cdot N = \frac{N_s^2 \mathcal{R}_1}{\mathcal{R}_T} \qquad (12)$$

$$L_m^\gamma = M \cdot T(\gamma) = \frac{N_p N_s \mathcal{R}_3}{\mathcal{R}_T} T(\gamma) \qquad (13)$$

where $\gamma = \{p, s\}$ defines the side of the T-model that the magnetizing inductance is referred to, $T(\gamma) = \{1/N, N\}$ is the corresponding turns ratio reflection function, and $N = N_s/N_p$ is the transformer turns ratio. It is clear from (11)-(13) that control of the magnetizing inductance, and both leakage inductances, can be achieved through manipulation of the number of turns and the three equivalent reluctances $\{\mathcal{R}_1, \mathcal{R}_2, \mathcal{R}_3\}$.

In light of (11)-(12), it should be noted that the designer has near-independent control of both leakage inductance in the T-model. One desirable configuration is the case shown in Fig. 4(a), where an air-gap is only placed on the leakage leg of the core. In this case, $\mathcal{R}_3 > \mathcal{R}_1 > \mathcal{R}_2$, where each inequality is assumed to present at least an order of magnitude between terms (i.e. $\mathcal{R}_3 > 10\mathcal{R}_1$). In many cases where a large magnetizing to leakage ratio is preferred, the factor by which $\mathcal{R}_3$ is greater than R_1 may be even larger. Therefore, (11)-(12) mathematically infer that the leakage inductance would be almost completely realized by the secondary-side (hereby deemed the EII Sec. configuration), as the leakage inductance on the primary-side would be small. Intuitively this is also clear, as the flux generated by the center-leg windings is more inclined to travel through the leakage leg, as compared to flux generated by the outer left leg windings, due to the relative magnitudes of $\mathcal{R}_1$ and $\mathcal{R}_2$. Naturally, other realizations are also possible where the leakage inductance could be nearly completely realized by the primary-side (e.g. exchanging the location of the primary and secondary-side windings in Fig. 3, henceforth referred to as the EII Pri.), or where the leakage distribution is closer to equal (e.g. by manipulating the core geometry through introducing air-gaps on the left- and center-leg such that $\mathcal{R}_2/\mathcal{R}_T \approx \mathcal{R}_1/\mathcal{R}_T$), though the latter configuration may result in reduced achievable L_m.
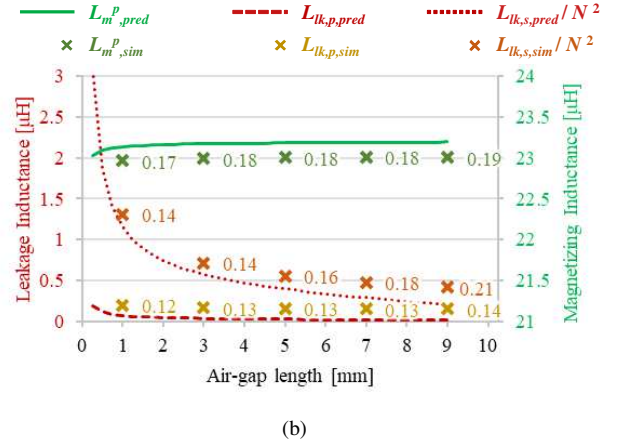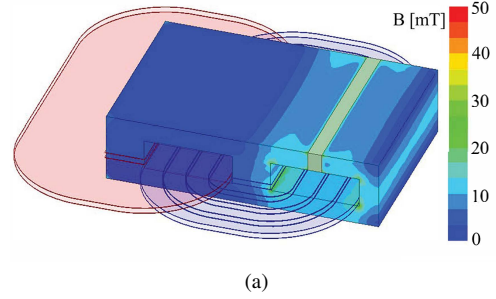

Fig. 5. 3D FEA simulations in Ansys Maxwell, (a) example core and winding configuration with overlaid core flux density in [mT], and (b) comparison of magnetizing and leakage inductance with predictions based on reluctance modelling. In (a), sinusoidal current excitations are applied with $I_p = 4\sqrt{2}$ A, and $I_s = \sqrt{2}$ A. In (b), the absolute value of inductance difference between the predictions and simulations are listed as labels for the simulation scatter-plots.

C. Comparison to Simulation

To validate the proposed reluctance modeling, a comparison between the predicted and simulated (via 3D FEA simulations in Ansys Maxwell) magnetizing and leakage inductances for an example EII transformer is evaluated. For simplicity, the conventional E58 core geometry [28] was considered, where the core's center leg width and outer right leg width were exchanged (i.e. l_{side} = 8.1 mm, and l_{lk} = 4.2 mm). This particular manipulation is preferred as the center and outer left legs generally carry more flux than the outer right leg, and hence larger cross-section areas along this path are beneficial for core loss reduction. An example core and winding structure is shown in Fig. 5(a), with the flux density overlaid within the core. In the presented simulation, the sinusoidal current relationship is $I_p(t) = nI_s(t)$, where the resulting flux in the core will isolate the leakage mechanism, as the magnetizing current is zero (cf. Fig. 1). It is clear that there is larger flux density in the outer right and center legs as a result of the dual role that the center leg realizes (i.e. the mutual flux path between primary and secondary, and the leakage flux path between the outer right leg and center leg). While the proposed simulation is beneficial for visualization of leakage generation within the transformer, practically magnetizing current will always exist, which is critical to consider in loss analyses.

The magnetizing and leakage inductances are compared as a function of the air-gap width in Fig. 5(b), with the absolute value of difference between the simulation and predictions
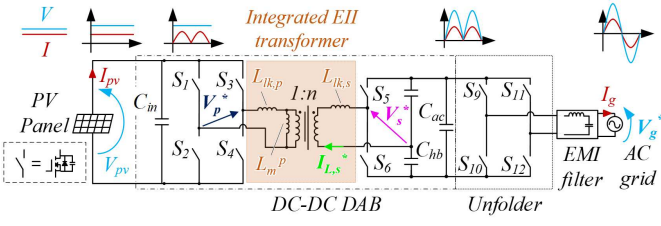
Fig. 6. Circuit schematic of the single-stage DC-AC microinverter based on the DAB circuit topology. The highlighted integrated EII transformer's leakage inductances are utilized for power transfer between the primary- and secondary-side. Waveforms probed in experimental measurements are bolded and marked with an asterisk.

TABLE II. NOMINAL OPERATING CONDITIONS OF THE MICROINVERTER.

$V_{in,mpp}$ [V]	$P_{in,mpp}$ [W]	$V_{ac,rms}$ [V]	f_{grid} [Hz]	f_{sw} [kHz]
40	400	240	60	200

plotted as a data label. From a qualitative perspective, the relationships between the magnetizing inductance and the air gap length are directly proportional, while the relationship between the dominant leakage inductance and the air gap length are inversely proportional, expected from (11)-(13). Furthermore, the secondary-side leakage inductance is dominant compared to the primary-side leakage inductance, expected due to the fact that $\mathcal{R}_1 > \mathcal{R}_2$. From a quantitative perspective, it is clear that the predicted and simulated values of magnetizing inductance agree very closely. On the other hand, there is some small error in both the primary- and secondary-side leakage inductance, with a near-uniform deviation of around 0.17 μH.

III. TRANSFORMER LOSS MODELING

A. Application to Dual-Active-Bridge

The proposed application of the EII transformer is a single-stage, single-phase, PV microinverter, based on the DAB topology shown in Fig. 6 [19]. The nominal specifications of the considered system are shown in Table II. In the considered topology, the leakage inductances act as the power transfer element between the primary- and secondary-side, while the magnetizing inductance can help to support zero-voltage-switching (ZVS) of the devices [23]. The considered control principle is phase-shift-based modulation, where in each switching period a quasi-square-wave voltage source can be applied on the primary-side and a square-wave voltage source can be applied on the secondary-side with a controllable phase shift; the transformer currents are hence decided according to the solution of the circuit in Fig. 1. Detailed analytical modelling in the frequency-domain regarding this control principle is well established, of which recent modelling efforts have been developed in [19] and [32].

B. Conduction Loss modeling

The conduction loss in the transformer can be calculated using the detailed formula,

$$P_{cond} = \frac{1}{2} \sum_{k=1,odd}^{k_{max}} \begin{bmatrix} \vec{I_{p,k}} & \vec{I_{s,k}} \end{bmatrix} \begin{bmatrix} R_p & R_m \\ R_m & R_s \end{bmatrix}_k \begin{bmatrix} \vec{I_{p,k}^*} \\ \vec{I_{s,k}^*} \end{bmatrix} \quad (14)$$

where $\vec{I_{p/s,k}}$ is the vector component of the primary- and secondary-side currents at the kth harmonic, R_p is the primary-side self-resistance, R_m is the winding mutual resistance, and R_s is the secondary-side self-resistance [24]. However, while (14) is the most accurate conduction loss expression, especially in dual-active-bridge converters where the transformer primary- and secondary-side currents are composed of multiple harmonic components, the analysis requires characterization of the resistance matrix of a transformer design across multiple harmonics of the switching frequency. The winding AC resistances as a function of frequency are difficult to derive analytically, which are generally due to both skin and proximity effects, conventionally calculated via Dowell's formula [25]- [26]. However, the proposed winding structure consists of both interleaved winding sections (where the AC resistance could be calculated more accurately), and non-interleaved winding sections (which do not obey Dowell's assumptions due to MMF variation in both the horizontal and vertical directions) [20]. As such, determination of the resistance matrix of a given design can only be reliably determined through the use of 3D FEA simulations [27]. Nevertheless, coordination between the optimization routine and 3D FEA simulations for each considered design would significantly increase the computational complexity of the analysis, and hence simplifications to (14) were pursued.

1) Conduction Loss Simplification (a): In light of the complexity issues regarding the use of (14), two approximations are proposed for computational simplification. First, the conduction loss at the kth harmonic is expanded into,

$$P_{c,k} = I_{p,k}^2 R_{p,k} + I_{s,k}^2 R_{s,k} + 2I_{p,k}I_{s,k}R_{m,k}\cos(\Delta\beta_k) \quad (15)$$

$$P_{cond} = \frac{1}{2} \sum_{k=1,odd}^{k_{max}} P_{c,k} \quad (16)$$

where $I_{p/s,k}$ is the magnitude of the primary- and secondary-side current at the kth harmonic, and $\Delta\beta_k$ is the phase angle difference between the currents. While the phase angle difference is easily known through circuit modelling, the derivation of the mutual resistance analytically is difficult. As such, the proposed approximation sets $2\cos(\Delta\beta_k) = 2$, effectively saying that the phase angle difference between the primary- and secondary-side currents is small enough to be ignored. The angular approximation is validated in Fig. 7(a) across the quarter-line-cycle at each CEC power level. It is clear that as the magnetizing inductance increases, the effect of the magnetizing current in perturbing the phase angle between the primary- and secondary-side is minimal. It is further evident that even for low magnetizing inductance of 10 μH, the approximation will only generate sufficient error in the low operating power levels. In these cases, specifically for negative R_m values, the predicted conduction losses will be slightly under-estimated.

2) Conduction Loss Simplification (b): The second approximation is proposed to promote a further simplification of the conduction loss calculation in (15). The calculation process is first given by,
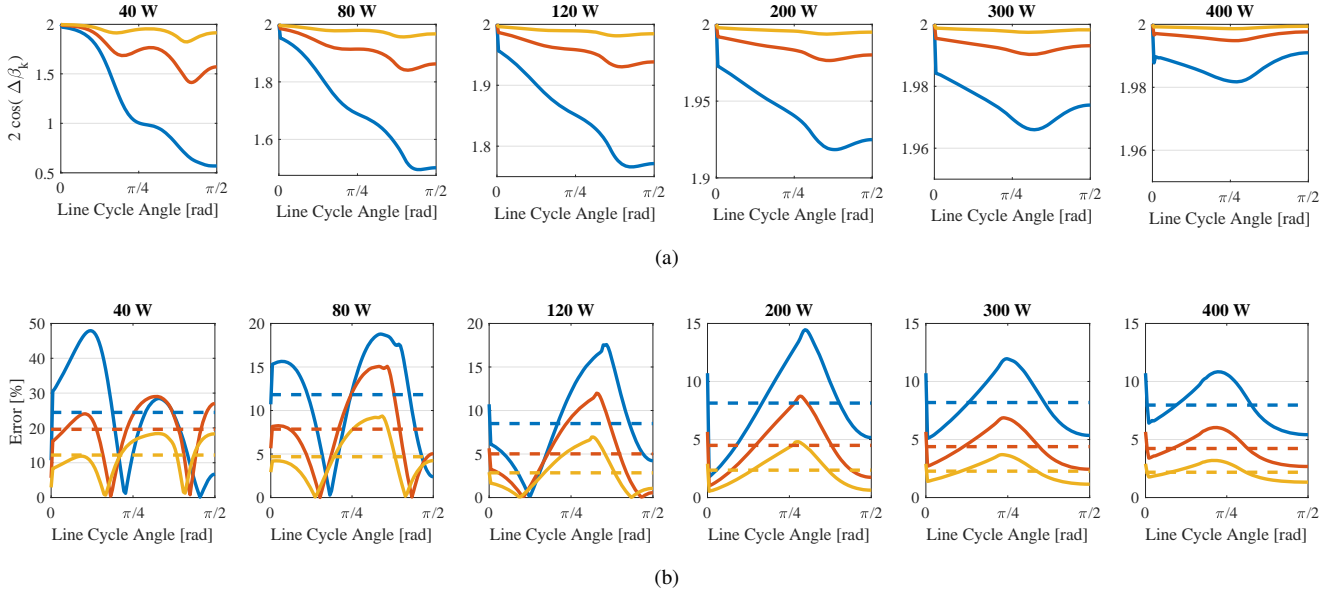
(a)

(b)

Fig. 7. Validation of approximation (a) $2\cos(\Delta\beta_1) \approx 2$, and (b) $I_{p,r,1} \approx nI_{s,r,1}$, for conduction loss calculation simplifications. In each case, the series of plots show the approximations across each CEC power level for an example 400 W microinverter, with $L_{lk,p} = 1.2$ μH and varying values of L_m^p. The blue, red, and yellow traces correspond to an L_m^p value of 10 μH, 20 μH, and 40 μH, respectively. In (b), the solid lines show local DC-DC operating point approximation error across the DC-AC line-cycle, whereas the dotted lines indicate the error in total line-cycle RMS.

$$P_{c,k} \approx I_{p,r,k}^2 R_{p,k} + I_{s,r,k}^2 R_{s,k} + 2I_{p,r,k}I_{s,r,k}R_{m,k} \quad (17)$$

$$P_{cond} = \sum_{k=1,odd}^{k_{max}} P_{c,k} \quad (18)$$

where the current magnitudes are replaced by the respective RMS value, through distribution of the factor of $\frac{1}{2}$ in (16). Under the approximation that $I_{p,r,k} \approx n \cdot I_{s,r,k}$, this expression can be rewritten as,

$$P_{c,k} \approx I_{p,r,k}^2 (R_{p,k} + R_{m,k}/n) + I_{s,r,k}^2 (R_{s,k} + nR_{m,k}) \quad (19)$$

where the $2I_{p,r,k}I_{s,r,k}R_{m,k}$ expression is split and summed separately into the first two terms. Whereas the first approximation discussed the phase angle between the two currents, the second approximation targets equal relative magnitudes of the two currents. An analytical analysis of the magnitude approximation is formulated in Fig. 7(b), where the error incurred by the approximation is analyzed across a quarter-line-cycle for each CEC power level. For each power level, the error of the assumption is calculated at each DC-DC operating point as well as across the line cycle. It is clear that for even $L_m^p = 10$ μH, errors in line-cycle RMS current are mostly below 10% despite certain DC-DC operating points having larger errors.

In general, both of the proposed approximations benefit in accuracy for larger ratios of magnetizing to leakage inductance, which is desirable in the proposed transformer design as the magnetizing flux path is ungapped. Specifically, large magnetizing inductances yield low magnetizing currents and hence generally lower core losses (of which the modelling is formulated in the following section). Furthermore, the approximation errors are largest in the lower power levels,

which are not as critical as the higher power levels (this will be more clear in Section IV-B in discussion of the CEC efficiency calculation). The two proposed approximations enable final restructuring of the conduction loss calculation into,

$$P_{cond} \approx \sum_{k=1,odd}^{5} I_{p,r,k}^2 \left(F_{r,p,k}R_{dc,p} + \frac{F_{r,s,k}R_{dc,s}}{n^2} \right) \quad (20)$$

where the first three odd harmonics are used for conduction loss calculation, $F_{r,p/s,k}$ is an equivalent primary- and secondary-side DC-to-AC resistance ratio at the kth harmonic including contributions of both the self and mutual resistances, and $R_{dc,p/s}$ are the primary- and secondary-side DC resistances. This form, facilitated by the balanced current approximations, is also shown under similar conditions in [24]. The formulation is beneficial for analytical procedures, as trends can be derived through detailed FEA simulation for the DC-to-AC resistance ratios, which are multiplied by simply formulated DC resistances. While the proposed balanced current approximations have been shown to be sufficiently accurate in the conditions surrounding the proposed application, they certainly are not uniformly applicable, especially in designs with reduced ratios of magnetizing to leakage inductance.

3) Design considerations: It is important to identify specific design trends associated with the formulation of the DC-to-AC resistance ratios, $F_{r,p}$ and $F_{r,s}$. Three unique transformer designs are analyzed in this sub-section with design parameters listed in the Appendix. In each case, the excitation frequency was fixed at 200 kHz, and the excitation amplitudes were 4 A_{rms} for the primary and 1 A_{rms} for the secondary. For each design, Fig. 8 demonstrates to-scale 3D FEA winding current distributions of the three designs, each with 5 mm for the distance between the leakage-leg air-gap and the windings beneath, deemed h_{gw} (cf. Fig. 4(a)).
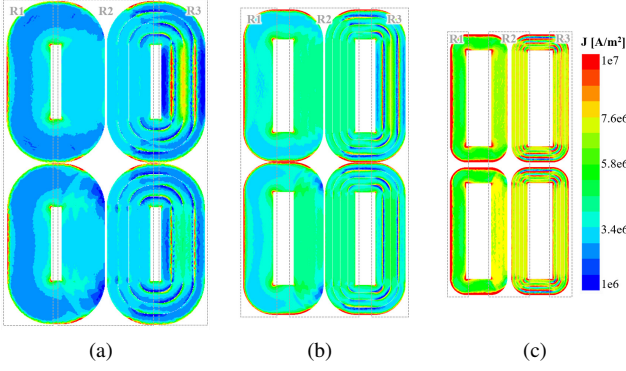
Fig. 8. Current density distributions to-scale for three designs under analysis, (a) transformer A, (b) transformer B, and (c) transformer C. Each of three unique regions (R1, R2, and R3) are highlighted for the three designs, where the current density has unique distribution patterns. The images in relationship to the winding stack-up from Fig. 3 are P-1 on the top-left, P-2 on the bottom-left, S-1 on the top-right, and S-2 on the bottom-right.
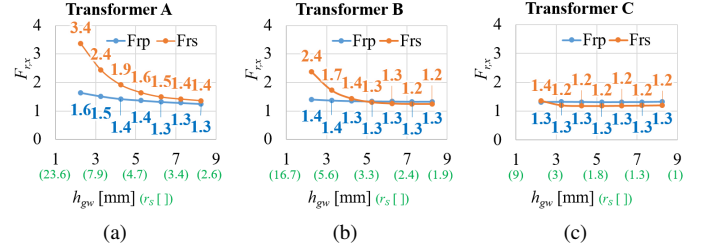

Fig. 9. Parametric analysis of the primary- and secondary-side DC-to-AC resistance ratios as a function of the air gap-to-winding distance (and Sullivan ratio in parenthesis) for, (a) transformer A, (b) transformer B, and (c) transformer C.
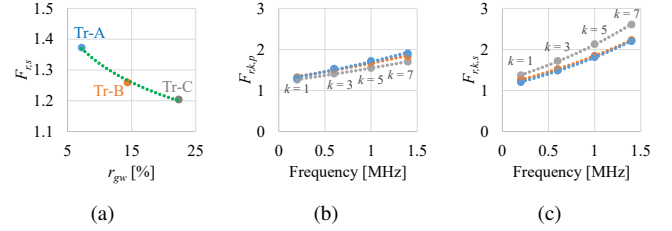

Fig. 10. Parametric analysis of the primary- and secondary-side DC-to-AC resistance ratios as a function of (a) the gap to winding width ratio for the secondary-side, (b) the frequency for the primary-side, and (c) the frequency for the secondary-side. Logarithmic trends are identified for the air-gap width to winding width ratio on the secondary-side, while exponential trends are identified for the resistance ratios as a function of frequency. Design details for Transformer A are shown in blue, Transformer B in orange, and Transformer C in gray.

The current distribution pattern in each case is consistent for each of the three indicated regions in Fig. 8, namely region 1 (R1) for the windings outside of the core footprint, region 2 (R2) for the interleaved winding portion, and region 3 (R3) for the winding portion beneath the leakage leg air-gap. First, region 1 indicates current concentration towards the edges of the windings. Next, region 2 exhibits very balanced current distribution, as this region has strong winding interleaving. Finally, region 3 exhibits current concentration in the winding portion beneath the air-gap, due to the H-field pattern that emanates from the air-gap, as indicated in [29] and [30].

Two key design insights regarding region 3 are important to investigate further, which also lead to determination of resistance trends in the other winding regions. First, while region 1 and region 2 realize similar current distribution patterns on each winding layer, the current distribution in region 3 is more uniformly distributed for the winding further from the gap than the winding closer to gap. This insight was also made in [17] for an inductor winding design. As such, it is inferred that the distance between the gap and windings, h_{gw} is an important parameter to be designed properly. In light of this, trends of h_{gw} versus $F_{r,p/s}$ are developed and plotted in Fig. 9. It is clear that for each transformer design, the secondary-side $F_{r,s}$ is a strong function of this gap distance up to a certain point, whereas the $F_{r,p}$ is relatively flat. A general rule of thumb that can be applied, which was originally proposed for inductor windings beneath an air-gap in [30], is that the ratio of w_{wind} to h_{gw} (hereby deemed the Sullivan ratio, r_S) should be less than or equal to four. In the case of the proposed transformer, of which only a single set of windings is below the gap, this rule of thumb is also quite accurate, which would lead to h_{gw} selections of $\sim$6 mm, $\sim$4 mm, and $\sim$2 mm for designs A, B, and C, respectively. Nevertheless, to ensure a closer-to-minimum $F_{r,s}$, the maximum bound of the Sullivan ratio is chosen to be three.

The second key insight is that the width of the crowding region is related to the width of the air-gap, implying that the ratio of the gap length to the winding width, $r_{gw} = l_{gap}/w_{wind}$ is an important design parameter. It should be noted that for a given transformer design, neither l_{gap} nor w_{wind} are free variables, and hence r_{gw} only serves to preferentiate one design over another. The values of the secondary-side DC-to-AC resistance ratios are shown as a function of r_{gw} in Fig. 10(a). It is clear that the value of $F_{r,s}$ varies quite significantly as a function of r_{gw}, and fits to a logarithmic trend (with an $R^2 = 0.9952$) of which the relationship is henceforth used. Specifically a logarithmic fit was considered due to the logarithmic spread of the perpendicular H-field component fringing from the gap to the windings [29].

Maintaining a Sullivan ratio of three, analysis of the DC-to-AC resistance ratios were further evaluated as a function of switching frequency harmonic. The results are presented for the primary-side DC-to-AC resistance ratio in Fig. 10(b), where the value varies exponentially in each case, increasing by roughly a factor of 10% for successive harmonic levels. Furthermore, the results for the secondary-side DC-to-AC resistance ratio are highlighted in 10(c), where again exponential trends are identified with increases of roughly a factor of 20% for successive harmonic levels. Therefore, the following resistance trends are utilized in the following multi-objective optimization,

$$F_{r,p,k} = 1.3 \cdot e^{0.055(k-1)} \tag{21}$$

$$F_{r,s,k} = (1.67 - 0.15 \ln(r_{gw})) \cdot e^{0.1(k-1)} \tag{22}$$

where the primary-side DC-to-AC resistance ratio of all designs is equal, whereas the secondary-side DC-to-AC resistance ratio is a function of the r_{gw} parameter.

C. Core Loss modeling

The proposed transformer structure exhibits non-uniform flux density due to the consideration of unique cross-section areas throughout the core, and the fact the flux in the three legs is non-equal. As such, a unique core-loss calculation procedure is developed, similar to that proposed in [15], broken down into three key steps. First, the equivalent circuit for a given switching period is analyzed based on the superposed harmonic analysis developed in [19], from which the time-domain currents on the primary- and secondary-side can be reconstructed. After reconstructing the time-domain equivalent currents, the flux in each of the transformer legs can be found as a function of excitation current from the transformer's reluctance model, with (5)-(7). Finally, the core loss can be calculated in each of the core's reluctance sections independently and summed using an adaptation of the improved Generalized Steinmetz Equation (iGSE) [21],

$$P_{core} = \frac{k_i}{T_{sw}} \left[\sum_{j=1}^{s} \left(\Delta B_{pp,j}^{\beta-\alpha} \sum_{i=1}^{d} \Delta t_i^{1-\alpha} \Delta B_{j,i}^{\alpha} V_j \right) \right] \quad (23)$$

$$\Delta B_{j,i} = \frac{\Delta \phi_{j,i}}{A_j} \quad (24)$$

where j corresponds to the core reluctance section (arbitrarily numbered from 1 to s); s corresponds to the maximum number of core sections considered; $\{k_i, \alpha, \beta\}$ are the Steinmetz parameters [21]; d is the number of unique time-steps that the switching period is discretized[1]; $\Delta B_{j,i}$ is the change in flux density in the discrete time step Δt_i; $\Delta B_{pp,j}$ is the peak-to-peak flux density of core section j across the switching period; and $\{A_j, V_j\}$ are the cross-section area and volume of the core section (cf. Table I).

The core loss modeling approach is validated using the Ansys Maxwell Magnetic Transient simulation, which allows arbitrary current excitation waveforms (determined from time-domain simulations of specific operating points) to be applied to the transformer windings. The simulation is then solved over several switching periods, where the average core loss can be extracted. An illustration of the core loss calculation process is highlighted in the top inset of Fig. 11. The transformer utilized for the analysis is that from Section II-C, with an air-gap length of 3 mm. The predicted core loss across the AC line cycle is compared to simulation at four example operating points for the 200 W average power level. The comparative results are shown in the bottom half of Fig. 11, where the simulation and model agree within 5% error in each case.

IV. MULTI-OBJECTIVE OPTIMIZATION OF CORE GEOMETRY

The proposed transformer is evaluated in a constrained multi-objective optimization procedure of the core geometry, to select a design with the lowest transformer efficiency drop

---

[1]In the considered primary-side full-bridge / secondary-side half-bridge topology there are at most six unique piece-wise linear portions of the transformer current [19].
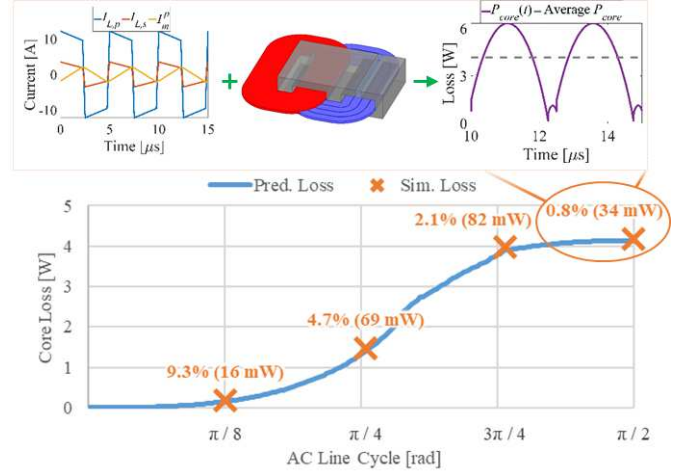

Fig. 11. Core loss simulation versus prediction at the 200 W average power level, with prediction error at the simulated points shown as a data label. The top inset highlights an example Ansys Maxwell Magnetic Transient simulation with user-defined current excitations applied to the core and winding geometry, which is solved over time to extract time-varying and switching period averaged core loss.

while satisfying power-throughput and size constraints, as explained below.

A. Design constraints

1) Parametric constraint: As detailed in [19], a target amount of leakage inductance is desired based on the maximum power transfer capability in the DC-AC DAB as well as limiting the conduction loss factor (CLF), which is a figure of merit denoting CEC-related conduction losses in the microinverter circuit. Generally, this constraint can be evaluated by checking,

$$C(1) = [L_{lk,s}(l_{gap}) = L_{lk,des} \; for \; l_{gap} \in \{0, l_{top}\}] \cdot \quad (25)$$

In other words, (25) evaluates whether or not the target leakage inductance can be generated by varying the air-gap length between zero and l_{top} (cf. Fig. 4).

2) Geometric constraints: Additional design constraints are posed regarding the footprint of the transformer, with the goal of optimizing power density assuming the rest of the PCB is pre-designed. The geometric constraints are pictorially shown in Fig. 12, where the PCB length should not be violated, and the transformer depth ensures at least that the power density requirement is met. Mathematically, the two geometric constraints are posed as,

$$C(2) = d_{core} + 2w_{wind} - D_{tr,max} \quad (26)$$

$$C(3) = l_{core} + w_{wind} - L_{tr,max} \quad (27)$$

where d_{core}, l_{core}, and w_{wind} are defined in Fig. 4, $D_{tr,max}$ and $L_{tr,max}$ are defined in Fig. 12, and the constraints are satisfied if the expression is less than or equal to zero. Dimensions of the PCB in Fig. 12 are highlighted in Table III, alongside other relevant specifications used to determine the maximum allowable transformer dimensions. A 5 mm increase in PCB length and depth was considered, as well as a 1 mm
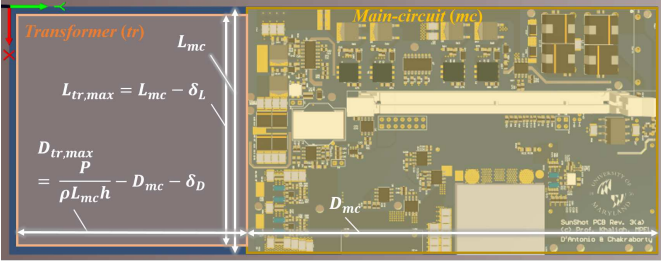
Fig. 12. Illustration of the transformer dimensional constraints in light of the main-circuit layout. Assuming the rest of the power circuit PCB has been pre-designed, the transformer length should not exceed the PCB length, while the maximum depth is decided according to the power density target and PCB height. Terms δ_D and δ_L denote additional margins on the allowable dimension.

TABLE III. SPECS. USED FOR TRANSFORMER FOOTPRINT CONSTRAINTS.

$L_{mc}(\delta_L)$ [mm]	$D_{mc}(\delta_D)$ [mm]	h (top / bottom) [mm]
90 (4)	150 (4)	25 (6 / 19)
ρ [W/cm^3]	$L_{tr,max}$ [mm]	$D_{tr,max}$ [mm]
0.6	87	83

increase in PCB height on the top and bottom, due to realistic implications of the microinverter packaging solution in the power density calculations. In the first iteration of the design optimization, the outer core geometry is considered to be fixed to that of the E58 core from Ferroxcube [28]. Section IV-E highlights extension of the design analysis to a fully custom core geometry.

In addition to constraints regarding the length and depth of the transformer footprint, additional constraints should be posed regarding the distance between the leakage leg air-gap and the windings below, in line with the discussion from Section III-B3. In particular, the ratio of winding width to the gap-to-winding distance should be less than or equal to three. This constraint can be posed mathematically as,

$$C(4) = \frac{w_{wind}}{h_{gw}} - 3 \qquad (28)$$

where w_{wind}, and h_{gw} are defined in Fig. 4, and the constraint is satisfied if the expression is less than or equal to zero.

B. Objective functions

In PV microinverter applications, the CEC efficiency is used to benchmark the circuit's efficiency performance. It is determined as a weighted sum of the circuit efficiency at various operating points,

$$\eta_{CEC} = \sum_{i=1}^{6} C_i \cdot \eta_i \qquad (29)$$

where the weighting coefficients are C = [0.04, 0.05, 0.12, 0.21, 0.53, 0.05], the power levels of interest are P = [10%, 20%, 30%, 50%, 75%, 100%]$P_{av,max}$, and η_i corresponds to the system efficiency at CEC power level i [22].

The converter's CEC efficiency in (29) can be decomposed to identify CEC percentage drops due specifically to the transformer,

$$\eta_{CEC} = \sum_{i=1}^{6} C_i \left[1 - \frac{(L_{core,i} + L_{cond,i} + L_{o,i})}{P_i} \right] \qquad (30)$$

where $L_{core,i}$ and $L_{cond,i}$ denotes the transformer's line-cycle-averaged core and conduction losses respectively, and $L_{o,i}$ represents the other losses in the system (i.e. device conduction, switching, etc.), at each average power level P_i.

The modulation-level optimization (MLO) developed in [19] is used to determine circuit behavior at 'N' number of DC-DC operating points across the symmetric DC-AC quarter-line cycle. In the utilization of the MLO, the time-domain transformer currents are hence known at every operating point for each CEC power level. As such, the core and conduction losses can be calculated at each DC-DC operating point according to the procedure described in Section III, and averaged across each CEC power level via,

$$L_{core,i} = \frac{1}{N} \sum_{1}^{N} P_{core}(I_p(t), I_s(t), \phi_1, \phi_2, \phi_3, A, V), \quad (31)$$

$$L_{cond,i} = \frac{1}{N} \sum_{1}^{N} P_{cond}(I_p(t), I_s(t), \vec{x}), \qquad (32)$$

where $I_p(t)$ and $I_s(t)$ are the time-domain expressions for the transformer terminal currents at each DC-DC operating point; $\phi_1 - \phi_3$ are expressions of the flux in each core leg (i.e. (5)-(7)); and $\{A, V\}$ are the areas of volumes of each core component from the detailed reluctance modeling (cf. Fig. 4(a)). With the loss expressions derived at each CEC power level, the optimization objective functions can be defined as,

$$\text{PCF} = Y(1) = \sum_{i=1}^{6} \frac{C_i}{P_i} L_{core,i}, \qquad (33)$$

$$\text{WLF} = Y(2) = \sum_{i=1}^{6} \frac{C_i}{P_i} L_{cond,i}. \qquad (34)$$

In particular, (33) describes the CEC efficiency drop due to core loss and is hence deemed the core loss factor (PCF), while (34) defines the CEC efficiency drop due to winding loss and henceforth is referred to as the winding loss factor (WLF). Together, the PCF and WLF add up to define the total CEC loss factor (TLF) of the transformer.

C. Optimization implementation

A flow-chart of the optimization procedure is shown in Fig. 13. In the first step, selection of core material, inductance targets, turns ratio, and dimensional constraints are input to the MATLAB-based program. A genetic algorithm (GA)-based multi-objective optimization procedure, which will be motivated in the following section, is used to navigate the three-dimensional search space consisting of the inner geometry parameters indicated in Fig. 4(a). For each set of

Input parameters :
1. Core material (FXC - 3F36)
2. Inductance target ($L_{lk,des}$)
3. Transformer turns ratio (n)
4. PCB dimensions ($L_{mc}, D_{mc}, \delta_L, \delta_D, h, \rho$)

End

Yes

Genetic-based iteration :
- Design space vector x_{1x3} or x_{1x6}

$x(1)$	$x(2)$	$x(3)$	$x(4)$	$x(5)$	$x(6)$
l_{side}	l_{lk}	h_{top}	l_{core}	d_{core}	h_{core}

No

'gamultiobj' stop condition eval.

No

Constraint analysis :
C(1). Achieve $L_{lk,des}$ with variation of l_{gap}
C(2-4). Geometric constraints satisfied

Yes

MLO at CEC operating points :
- Utilize n and achieved $\{L_{lk,p}, L_{lk,s}, L_m\}$
- For each P_i determine $\theta_i(t)$ and $\delta_i(t)$
- Calculate $P_{core,i}$ and $P_{cond,i}$

Objective function calculation :
PCF $= Y(1) = \Sigma (C_i/P_i) \cdot L_{core,i}$
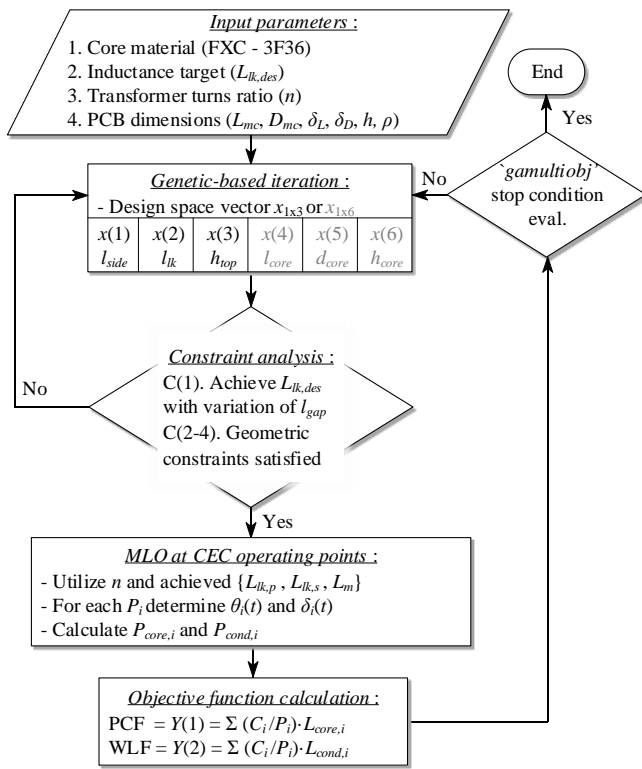WLF $= Y(2) = \Sigma (C_i/P_i) \cdot L_{cond,i}$

Fig. 13. Flow chart for facilitating the multi-objective optimization routine for the proposed EII transformer. Definition of the input vector is indicated in the iteration block in coordination with Fig. 4.

design parameters $\vec{x}_{1x3}$, the constraints from Section IV-A are evaluated. If the constraints are not met, the genetic algorithm re-iterates the design variables; else, the algorithm proceeds to calculate the objective functions according to the analysis in Section IV-B. The multi-objective optimization procedure thereafter seeks to identify the trade-off between core and conduction losses of the transformer, as they impact the CEC efficiency drop. The algorithm proceeds until the stop conditions associated with MATLAB's in-built multi-objective GA routine 'gamultiobj' are met, typically limited either by the number of generations or the relative change in Pareto candidates between generations. In addition to the EII transformer, the shell and ACL transformers with $m_p = 1$ and $m_s = 4$ from Fig. 2(b) and (c), respectively, were analyzed for optimal geometric configurations.

D. Results

The results of the optimization procedure for the ACL transformer, shell transformer, and three variants of the EII transformer are depicted in the Pareto chart in Fig. 14(a). The shell and ACL transformer with less number of primary turns were not considered due to difficulty in achieving the leakage inductance target, or too high core flux density. In general, the trade-off between core and conduction loss is clear from the convexity of the Pareto curves towards the bottom-left corner. The size of each Pareto indicator is proportional to the footprint area of the transformer, where it is clear that the designs with larger footprint tend to have lesser conduction

loss at the cost of increased core loss due to the usage of larger winding widths, which overhang from the core in multiple dimensions (cf. Fig. 2 and Fig. 3). One key takeaway from Fig. 14(a) is that the EII transformer designs with $N_p = 2$ perform better than the ACL transformer, specifically as a result of lesser CEC drop due to core loss (near uniform left shift in the Pareto front). On the other hand, the shell transformer suffers from much higher conduction losses than the EII designs with $N_p = 2$ due to the non-interleaving pattern of the windings. The performance of the shell transformer is similar to that of the EII with $N_p = 3$, though the EII still achieves lower core losses and slightly lower conduction losses in certain configurations, as the DC-to-AC resistance ratio in the EII is reduced in comparison to the shell. Finally, in comparison to a low-leakage transformer with a separate inductor in series on the primary-side, the EII transformers outperform from a loss perspective but are realized in a slightly larger total footprint area. The reduced loss in the EII is primarily due to reduced conduction losses, with a balance of core losses, as the non-integrated transformer with a series inductor requires independent winding sets for each magnetic component.

To determine the ideal candidate to pursue experimentally, the total transformer CEC drops for each of the Pareto candidates are shown in Fig. 14(b). It is clear in this case that the lowest loss designs for the EII configurations are lower than that in each of the other configurations. Indicated transformer designs T_1-T_4, representing the lowest loss designs for each transformer type, are summarized in Table IV. It is concluded that the EII transformer with $N_p = 2$ has the best performance, regardless of whether the leakage is lumped on the primary and secondary sides. As such, the decision of where to lump the leakage inductance can come from secondary considerations, such as zero-voltage-switching (ZVS), and a more comprehensive analysis can certainly explore those effects. However, since the focus of this paper was to highlight the key advantages of the EII approach, optimal leakage distribution has not been investigated in this work. Finally, it may be noted that in addition to achieving the lowest loss, the EII transformer also has a lower footprint area than the optimal shell and ACL designs due to the reduced winding overhang outside of the core footprint.

One additional point of analysis for the EII Sec. transformers with $N_p = 2$ is highlighted in Fig. 14(c), where the total transformer drop of each Pareto candidate is broken down by loss mechanism. It is interesting to note that the total transformer drop is relatively constant within a range of Pareto candidates, around 1.2%. However, this total drop is achieved with differing proportions of core and winding losses. The T_4 selection achieves a more balanced distribution of core and winding losses, though there is freedom to select a design in which the loss is more skewed to the core ($T_{4,core}$) or windings ($T_{4,cond}$). This implies that the decision of which design to select can come from other practical design perspectives, predominantly thermal management. In many cases, due to the large area of the core and the fact that the windings are embedded into the PCB, a larger core loss may be preferable for cooling.
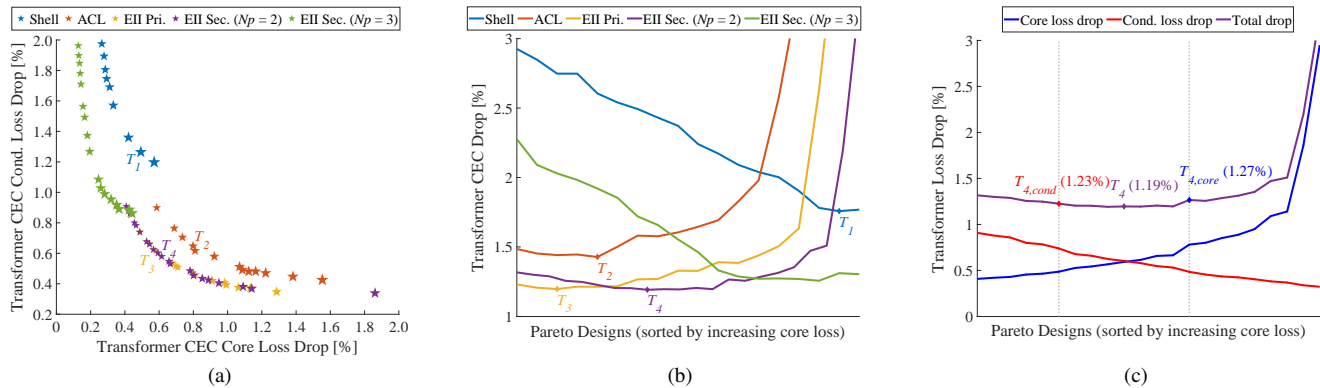
Fig. 14. Results of the multi-objective optimization procedure of the considered integrated transformers, (a) Pareto chart, (b) total loss breakdown of Pareto candidates sorted by increasing core losses, and (c) breakdown of the EII Sec. (N_p = 2) Pareto candidates by loss mechanism. The size of the stars in the Pareto chart in (a) are proportional to the footprint area of the design. The indicated design points T_1-T_4 are highlighted in Table IV.

TABLE IV. COMPARISONS OF OPTIMAL E58 TRANSFORMER DESIGNS. DEFINITIONS OF PCF AND WLF ARE PROVIDED IN (33) AND (34).

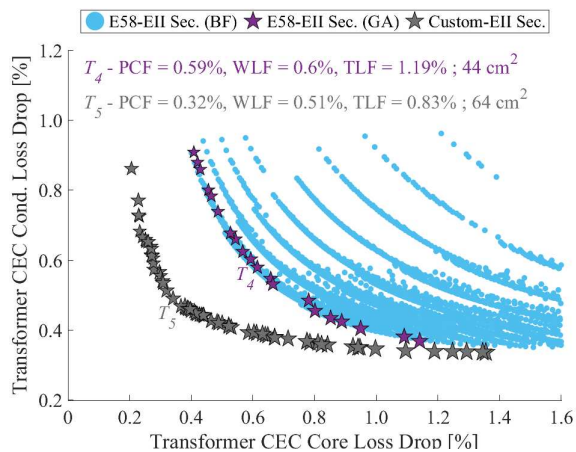| Transformer Type	L_m^p [μH]	$L_{lk,p}$ [μH]	$L_{lk,s}$ [μH]	PCF [%]	WLF [%]	TLF [%]	Footprint Area [cm^2]	Intra-overlap	Inter-overlap
Ind. + Tr. — T_0	20	1.18	n/a	0.12%	1.04%	1.16%	40.6 (8.15-i + 32.5-t)	Low	High
Shell [14] — T_1	27.7	0.58	0.58	0.49	1.26	1.75	66.1	High	Low
ACL [15] — T_2	39.2	0.6	0.6	0.81	0.62	1.43	48.4	Medium	High
EII Pri. [Proposed] — T_3	40.4	1.17	0.05	0.58	0.62	1.2	41.3	Low	Medium
EII Sec. [Proposed] — T_4	38.6	0.07	1.2	0.59	0.6	1.19	42.2	Low	Medium

Fig. 15. Pareto-front comparison between the E58-EII Sec. and the Custom-EII Sec. Furthermore, utilization of GA is justified, as the BF- and GA-derived Pareto fronts are nearly identical for the E58 core analysis.

E. Extension to Custom Core Geometry

To facilitate a fully custom core analysis, three additional design parameters (outer core width, length, and height) can be introduced, where the design vector from Fig. 13 is hence 6-dimensional, $\vec{x}_{1x6}$. Due to the dimensionality of the fully custom problem, and the inner-loop being computationally expensive, use of GA is invaluable; the computation time would be very high considering brute-force (BF) approaches (i.e. an exhaustive decision space search) that scale according to $t_{ex}n^d$, where t_{ex} is the execution time of one iteration, n is the dimension of the decision space vector, and d is the number of discrete possibilities of each design variable.

The results and comparison of the fully custom EII Sec.

analysis (Custom-EII Sec.), versus the E58-EII Sec., is highlighted in Fig. 15. In this figure, an overlay of the BF analysis for the E58-EII Sec. transformer was performed to compare against the GA-based implementation. It is shown that the GA (total time = 36.27 hrs.) is capable of delivering near-optimal results based on the BF search (total time = 31.8 hrs.), at a similar total execution time. Importantly, the BF decision space contained 25 points for x_1 and x_2, and 5 points for x_3 (cf. Fig. 13 for variable identification), while the GA was executed to 100 generations at most. On the other hand, the fully custom design (total GA run time = 100.8 hrs.) Pareto front is nearly intractable with a BF-based search, where 25 points for the additional three input parameters $\{x_4, x_5, x_6\}$ would create a decision space with over 48 million unique designs.

Comparing transformers T_4 and T_5 in Fig. 15, allowing all of the core dimensions to be variable enables a reduction in efficiency drop by almost 0.4%. However, for the reduction in loss attributed primarily to reduced core loss, the footprint area of the transformer increases by roughly 50%. Nevertheless, the proposed optimization procedure ensures that the circuit power density target is still maintained. The finally selected EII Sec. designs T_4 and T_5 are presented in Table V, alongside predictions from 3D FEA simulation. It is clear that in both cases the predictions of magnetizing and leakage inductance agree well, further validating the transformer characterization from Section II. Additionally, the AC resistance predictions in the model are within 5% of the 3D FEA results. Comparing the CLF with the analytically simplified approach in (20) versus use of (14), where the resistance matrix was extracted from 3D FEA simulations (14), yielded an absolute difference of 0.01% for T_4 and 0.008% for T_5, validating the proposed AC resistance modelling and associated simplifications.

TABLE V. GEOMETRIC AND ELECTRICAL SPECIFICATIONS OF THE OPTIMAL E58-EII SEC. TRANSFORMER WITH $N_P = 2$ (T_4), AND THE OPTIMAL CUSTOM-EII SEC. (T_5). DIMENSIONS PROVIDED IN [MM]. ELECTRICAL PARAMETERS ARE COMPARED TO 3D FEA SIMULATION VALUES IN PARENTHESIS.

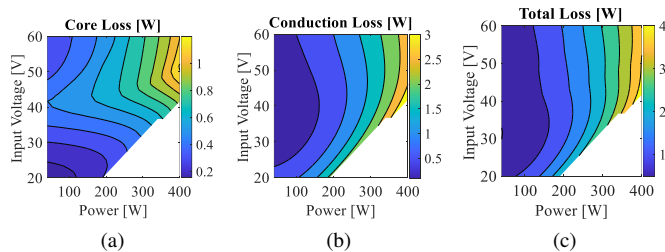| Design	l_{side}	l_{lk}	h_{top}	l_{gap}	l_{core}	d_{core}	h_{core}	R_{dc} [mΩ]	$R_{ac,1}$ [mΩ]	L_m^p [μH]	$L_{lk,sec}$ [μH]
T_4	11.3	13.4	4.9	1.4	58.4	38.1	15.4	10.9 (10.5)	13.64 (13.59)	38 (39)	1.28 (1.2)
T_5	10.5	6.2	6.0	2.35	60.6	49.9	18.6	9.26 (9.35)	12.05 (12.08)	43.6 (43.9)	1.23 (1.25)

(a)   (b)   (c)

Fig. 16. Extended loss analyses of the T_5 transformer across a range of input voltage and power transfer conditions, where analytical calculations were performed for (a) core losses, (b) conduction losses, and (c) total losses. The white regions of the loss contours are infeasible operating points due to the maximum power transfer condition of the DAB converter with a fixed switching frequency [19].

F. Extension of Operation Space

In microinverter applications, it is typical that the operating point of the solar panels vary uniquely from the nominal operating conditions across each day of the year due to changing temperatures, irradiation, and presence of partial shading conditions. While these details were not explicitly considered in the optimization process, the optimally selected T_5 transformer performance was validated across a wide range of operating points. The transformer core and conduction losses were analytically verified for an array of input voltages, namely 20 V to 60 V, with power levels between 40 W and 400 W, with results shown in the contour plots in Fig. 16. It is clear that the losses are quite uniform between the 20 V and 60 V operation cases across all power levels.

V. EXPERIMENTAL RESULTS

A. Transformer characterization

The selected EII Sec. transformer designs for the E58 (T_4) and custom design (T_5) from the previous section, each shown in Fig. 17, were fabricated by a Ferrite core manufacturer and evaluated for their electrical characteristics. Due to the fact that the magnetizing flux path is realized with an un-gapped core, it is first important to characterize the permeability of the core, as the material permeability is only guaranteed within $\pm 20\%$ [31], and additional effects at the core interfaces may attribute to additional permeability reduction. A unique experimental value of permeability was extracted for each core, as they were produced in separate batches. The effective permeability of the E58 core was concluded to be $\mu_r = 950$, while the effective permeability for the custom core was $\mu_r = 1250$.

Using the calibrated permeability, the transformer's electrical characteristics were compared to predictions and 3D FEA simulations. The results of the comparison are highlighted in Table VI. Due to the permeability reduction, the achieved magnetizing inductance is less than the value expected considering the nominal permeability value (cf. Table V). This
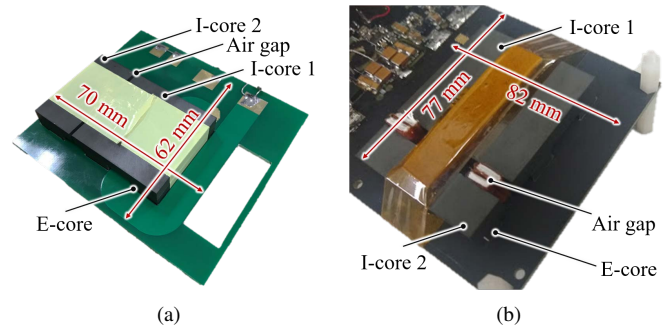

(a)   (b)

Fig. 17. Annotated photograph of the assembled EII Sec. transformers (a) E58-based design (T_4), and (b) custom core design (T_5). In each design, the core gap is controlled with a unity permeability shunt, and compressed with tape. In (b), an additional rigid sheet is placed on the top of the core for assembly support.

TABLE VI. EXPERIMENTAL ELECTRICAL PARAMETERS OF T_4 AND T_5.

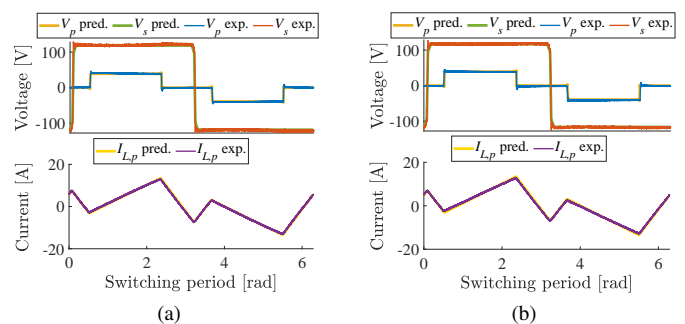| Transformer	L_m^p [μH]		$L_{lk,p}$ [μH]		$L_{lk,s}$ [μH]	
	Sim.	Exp.	Sim.	Exp.	Sim.	Exp.
T_4	22.3	22.8	0.27	0.38	0.92	0.91
T_5	38.7	37.6	0.34	0.36	0.97	0.95

(a)   (b)

Fig. 18. Comparison between predicted and experimental behavior of the main-circuit at an example DC-DC operating point with, (a) E58-EII Sec. T_4, and (b) Custom-EII Sec. T_5. The demonstrated waveforms are indicated in Fig. 6

may increase conduction losses due to increased RMS current, however there is no significant penalty to core loss, as the flux density in the ungapped magnetizing flux path is proportional to μ_r (cf. (5)-(7)). Nevertheless, comparison of the transformer experimental parameters to prediction and 3D FEA simulation is accurate with the proper value of permeability, validating the transformer modelling.

B. Hardware testing

The EII transformer prototypes were connected to a microinverter circuit with the specifications in Table II to verify the effectiveness of the proposed design under nominal power
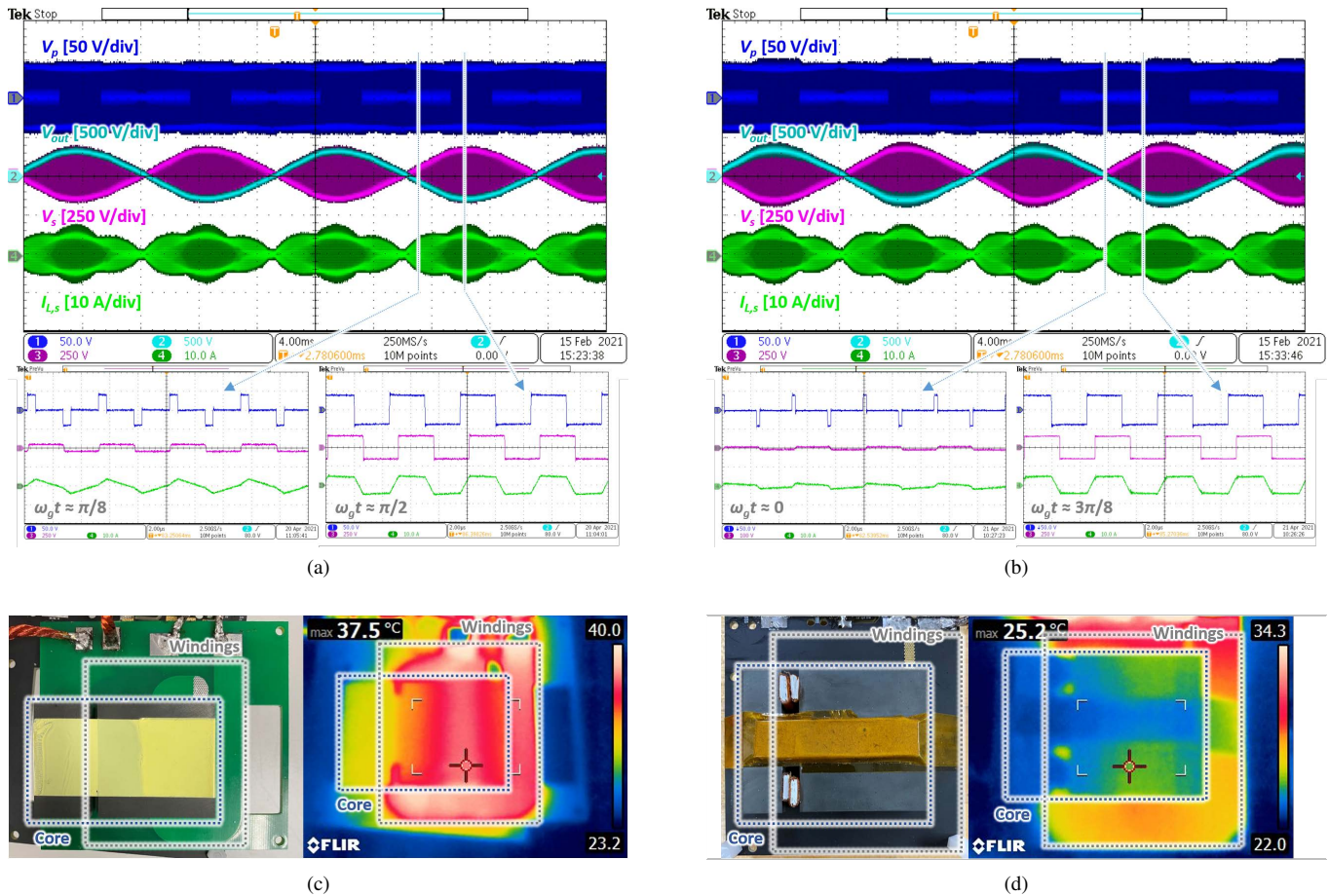
(a)

(b)

(c)

(d)

Fig. 19. Circuit performance at the 300 W average power level, (a) low-frequency waveforms with T_4 and high-frequency zoom-in near $\omega_g t = \pi/8$ and $\omega_g t = \pi/2$, (b) low-frequency waveforms with T_5 and high-frequency zoom-in near $\omega_g t = 0$ and $\omega_g t = 3\pi/8$, (c) clear and thermal images of T_4 transformer, and (d) clear and thermal images of T_5 transformer. The demonstrated waveforms in (a) and (b) are indicated in Fig. 6.

transfer conditions. The circuit uses a combination of GaN-based devices (EPC2001C) on the primary-side, and Si-based devices on the secondary-side (IPD60R180P7) and unfolder bridge (TK290P60Y). Further details regarding circuit design insights and modulation-level analyses can be found in [19] and [32].

1) DC-DC testing: The transformers were first connected to the main-circuit in which a steady-state DC-DC converter operation was analyzed. The resulting waveforms are shown in Fig. 18, including an overlay of predicted and experimental waveforms plotted in MATLAB. The electrical characterization of both the T_4 and T_5 designs is verified, as the experimental and predicted waveforms (evaluated via the approach in [32]) nearly completely overlap. Furthermore, the transformer current waveforms do not exhibit significant ringing at the primary or secondary switching transitions, implying that the parasitic capacitances of the prototype are adequately mitigated.

2) DC-AC testing: The transformer was next evaluated in DC-AC operation for both electrical and thermal performance. In all experimental scenarios the DC input voltage was set to 40 V, and the modulation parameters were determined offline and delivered to the devices through the use of look-up tables (LUTs). The low-frequency electrical waveforms with a resis-

tive load at the 300 W operating condition are shown using T_4 and T_5 in Fig 19(a)-(b), respectively. The two low-frequency waveforms are nearly identical and demonstrate good sinusoidal output voltage shaping, as the leakage inductance is controlled to be roughly equal between the two designs and the modulation parameters delivered to the devices were the same. In addition to the low-frequency circuit behavior, several high-frequency zoom-in waveforms are shown at various grid angles ($\omega_g t$), namely $\omega_g t = \{\pi/8, \pi/2\}$ for T_4 and $\omega_g t = \{0, 3\pi/8\}$ for T_5, are also provided in 19(a)-(b) to further demonstrate the phase-shift control principle as well as the transformer performance across a range of operating points. The DC-DC waveforms were selected differently for each transformer to provide insight into the transformer performance across a wide range of secondary-side voltage levels and modulation conditions, as it was already established in Fig. 18 that the performance of both transformers is largely equivalent for similar DC-DC operating points.

Thermal images, captured using a FLIR E6 infrared camera for both prototypes, are shown in Fig. 14(c)-(d). It can be observed that for the T4 design in Fig. 19(c), the core hot spot temperature was 37.5 °C along the core region where the primary- and secondary-side windings overlap. This is due in part to indirect heating from the windings, as well as highest
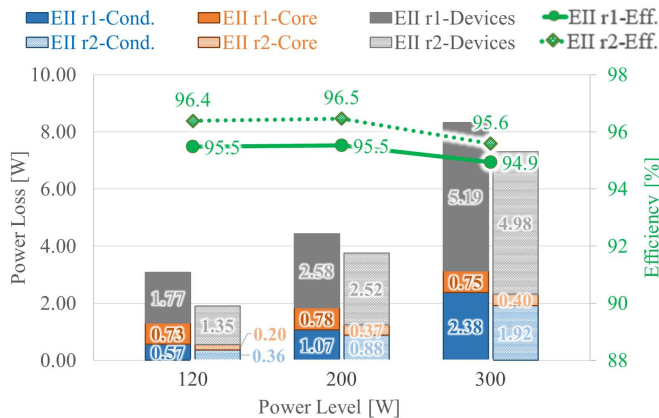
Fig. 20. Experimental efficiency of the microinverter with the expected loss breakdown between the transformer and devices at each power level.

TABLE VII. TRANSFORMER DESIGN PARAMETERS CONSIDERED FOR CONDUCTION LOSS ANALYSES.

Tr	l_{side} [mm]	d_{core} [mm]	w_{wind} [mm]	l_{gap} [mm]	r_{gw} [%]
A	5	38.6	23.1	1.7	7.2
B	10.5	49.9	16.2	2.4	14.4
C	12.5	49.9	8.45	2	22.3

core loss density in this segment of the core as the cross-section area is the lowest in the magnetizing flux path. In comparison, the T_5 transformer in Fig. 19(d) exhibits significantly reduced core temperatures at 25.2 °C, while the surrounding windings reached $\sim$ 29 °C. The reduced temperatures in both the core and windings exemplify improved loss performance of T_5.

3) Efficiency analysis: The efficiency of the circuit was analyzed at the 120 W, 200 W, and 300 W average power levels, as they contribute most significantly to the microinverter's CEC efficiency. The results of the efficiency characterization are shown in Fig. 20, where a peak efficiency of 96.5% is achieved at the 200 W power level with the T_5 transformer. Generally, up to 1% efficiency improvement is realized with the T_5 transformer compared to T_4. In addition to the general efficiency number, the predicted loss contributions from the transformer core, windings, and devices are shown as clustered columns on Fig. 20. It is evident that reduction of core loss is a principal contributor to improved efficiency with T_5.

VI. CONCLUSION

This manuscript has presented a novel planar-based integrated transformer concept and optimal design comparison to other similar transformers from literature. The proposed transformer achieves asymmetrically distributed controllable leakage inductance through an independent core leg, where a horizontal air gap is used for reluctance control. Closed-form expressions of the core and winding losses of the proposed design in a DC-AC single-stage microinverter topology are developed and combined with the reluctance modelling in a multi-objective design optimization of the transformer geometry. Extending the design optimization to other integrated transformers from literature revealed benefits in the proposed structure from the perspectives of transformer efficiency (specifically regarding controlled AC resistance and low core losses), footprint area, and parasitic capacitance, alongside simple winding layout and manufacturability. The proposed transformer design was then analyzed considering a fixed outer geometry versus a fully custom geometry, where a theoretical 0.4% CEC efficiency improvement (from 1.19% to 0.83%) could be achieved at the cost of increased footprint area. Based

on the design analyses, two optimal transformer prototypes were connected to a DC-AC microinverter circuit, and a peak efficiency of 96.5% was achieved.

APPENDIX

A. Transformer Designs in P_{cond} Analysis

In developing the analytical framework regarding the DC-to-AC side resistance ratios, three unique transformer designs were considered that realized a wide variation across the design space. These three designs were informed from the custom transformer multi-objective design analysis in Section IV-E. With reference to the Pareto front in Fig. 15, Transformer A is one of the bottom-right corner designs with a PCF of 1%, Transformer B is the finally selected design T_5, and Transformer C is the design in the upper-left corner. Key design specifications related to conduction losses are highlighted in Table VII, where clearly the designs have unique values geometric variables as well as r_{gw}.

ACKNOWLEDGMENT

REFERENCES

[1] A. Khaligh and M. D'Antonio, "High-performance Planar Integrated-transformer for Isolated Converter Systems", U.S. Provisional Patent Application No. 63/113,185, Nov. 12, 2020.

[2] J. Biela and J. W. Kolar, "Electromagnetic integration of high power resonant circuits comprising high leakage inductance transformers," in *Proc. IEEE 35th Annu. Power Electron. Spec. Conf.*, 2004, vol. 6, pp. 4537–4545.

[3] A. J. Hanson and D. J. Perreault, "Modeling the Magnetic Behavior of N-Winding Components: Approaches for Unshackling Switching Superheroes," in *IEEE Power Electron. Mag.*, vol. 7, no. 1, pp. 35-45, Mar. 2020.

[4] S. Yu, C. Hsiao and J. Weng, "A High Frequency CLLLC Bi-directional Series Resonant Converter DAB Using an Integrated PCB Winding Transformer," in *Proc. IEEE 35th Ann. Appl. Power Electron. Conf. Expo.*, New Orleans, LA, USA, 2020, pp. 1074-1080.

[5] Y. Liu, H. G. Wu, J. Zou, Y. Tai and Z. Ge, "CLL Resonant Converter with Secondary Side Resonant Inductor and Integrated Magnetics," in *IEEE Trans. on Power Electron.*, doi: 10.1109/TPEL.2021.3074646.

[6] M. H. Ahmed, A. Nabih, F. C. Lee and Q. Li, "Low-Loss Integrated Inductor and Transformer Structure and Application in Regulated LLC Converter for 48-V Bus Converter," in *IEEE J. of Emerg. and Sel. Topics in Power Electron.*, vol. 8, no. 1, pp. 589-600, March 2020.

[7] Z. Ouyang, W. G. Hurley and M. A. E. Andersen, "Improved Analysis and Modeling of Leakage Inductance for Planar Transformers," in *IEEE J. of Emerg. and Sel. Topics in Power Electron.*, vol. 7, no. 4, pp. 2225-2231, Dec. 2019.

[8] Z. Ouyang, O. C. Thomsen and M. A. E. Andersen, "The analysis and comparison of leakage inductance in different winding arrangements for planar transformer," in *Proc. 2009 International Conference on Power Electronics and Drive Systems (PEDS)*, Taipei, 2009, pp. 1143-1148.

[9] Y. Park, S. Chakraborty and A. Khaligh, "A Bare-die SiC-based Isolated Bidirectional DC-DC Converter for Electric Vehicle On-board Chargers," in *Proc. 2020 IEEE Transportation Electrification Conference & Expo (ITEC)*, Chicago, IL, USA, 2020, pp. 49-54.

[10] M. Mu, L. Xue, D. Boroyevich, B. Hughes and P. Mattavelli, "Design of integrated transformer and inductor for high frequency dual active bridge GaN Charger for PHEV," in *Proc. IEEE 30th Ann. Appl. Power Electron. Conf. Expo.*, Charlotte, NC, 2015, pp. 579-585.

[11] M. A. Bakar and K. Bertilsson, "An improved modeling and construction of power transformer for controlled leakage inductance," in *Proc. 2016 IEEE 16th International Conference on Environment and Electrical Engineering (EEEIC)*, Florence, 2016, pp. 1-5.

[12] J. Zhang, Z. Ouyang, M. C. Duffy, M. A. E. Andersen, and W. G. Hurley, "Leakage Inductance Calculation for Planar Transformers With a Magnetic Shunt," in *IEEE Trans. on Ind. Applicat.*, vol. 50, no. 6, pp. 4107–4112, Nov. 2014.

[13] Y. Liu, X. Huang, Y. Dou, Z. G. Ouyang and M. A. E. Andersen, "GaN-based ZVS Bridgeless Dual-SEPIC PFC Rectifier with Integrated Inductors," in *IEEE Trans. on Power Electron.*, doi: 10.1109/TPEL.2021.3070961.

[14] J. Biela and J. W. Kolar, "Analytic Model Inclusive Transformer for Resonant Converters Based on Extended Fundamental Frequency Analysis for Resonant Converter-Design and Optimization," in *IEEJ Trans. IA*, vol. 126, no. 5, pp. 568–577, 2006.

[15] B. Li, Q. Li and F. C. Lee, "High-Frequency PCB Winding Transformer With Integrated Inductors for a Bi-Directional Resonant Converter," in *IEEE Trans. on Power Electron.*, vol. 34, no. 7, pp. 6123-6135, July 2019.

[16] Y. Kim, C. Kim, K. Cho, K. Park and G. Moon,"ZVS phase shift full bridge converter with controlled leakage inductance of transformer," in *Proc. INTELEC 2009 - 31st International Telecommunications Energy Conference*, Incheon, 2009, pp. 1-5.

[17] S. Mukherjee, Y. Gao and D. Maksimović, "Reduction of AC Winding Losses Due to Fringing-Field Effects in High-Frequency Inductors With Orthogonal Air Gaps," in *IEEE Trans. on Power Electron.*, vol. 36, no. 1, pp. 815-828, Jan. 2021.

[18] J. Muhlethaler, J. W. Kolar and A. Ecklebe, "A novel approach for 3d air gap reluctance calculations," in *Proc. 8th International Conference on Power Electronics - ECCE Asia*, Jeju, 2011, pp. 446-452.

[19] M. D'Antonio, S. Chakraborty, and A. Khaligh, "Design Optimization for Weighted Conduction Loss Minimization in a Dual-Active-Bridge-Based PV Microinverter," in *Proc. 2020 IEEE Energy Convers. Congr. and Expo.*, Oct. 2020, pp. 6008–601.

[20] N. Dai and F. C. Lee, "Edge effect analysis in a high-frequency transformer," in *Proc. of 1994 Power Electronics Specialist Conference - PESC'94*, Vol. 2, pp. 850–855 vol.2, 1994.

[21] K. Venkatachalam, C. R. Sullivan, T. Abdallah and H. Tacca, "Accurate prediction of ferrite core loss with nonsinusoidal waveforms using only Steinmetz parameters," in *Proc. 2002 IEEE Workshop on Computers in Power Electronics*, Mayaguez, Puerto Rico, USA, 2002, pp. 36-41.

[22] W. Bower, C. Whitaker, W. Erdman, M. Behnke, and M. Fitzgerald, *Performance Test Protocol for Evaluating Inverters Used in Grid Connected Photovoltaic Systems.* Albuquerque, NM: Sandia Nat. Lab., Oct. 2004.

[23] J. Everts, F. Krismer, J. Van den Keybus, J. Driesen, and J. W. Kolar, "Charge-based ZVS soft switching analysis of a single-stage dual active bridge AC-DC converter," in *Proc. 2013 IEEE Energy Convers. Congr. and Expo.*, Sep. 2013, pp. 4820–4829.

[24] J. H. Spreen, "Electrical terminal representation of conductor loss in transformers," in *IEEE Trans. on Power Electron.*, vol. 5, no. 4, pp. 424-429, Oct. 1990.

[25] P.L. Dowell, "Effects of eddy currents in transformer windings", in *Proc. of the IEEE*, vol. 113, no. 8, pp. 1387–1394, Aug. 1966.

[26] J. A. Ferreira, "Improved analytical modeling of conductive losses in magnetic components", in *IEEE Trans. on Power Electron.*, vol. 9, no. 1, pp. 127–131, Jan. 1994.

[27] D. R. Zimmanck and C. R. Sullivan, "Efficient calculation of winding-loss resistance matrices for magnetic components," in *Proc. IEEE Workshop Comput. Power Electron.*, 2010, pp. 1-5.

[28] "E58/11/38 - Data sheet," Ferroxcube, Sept. 2008. [Online]. Available: http://ferroxcube.home.pl/prod/assets/e581138.pdf.

[29] W. A. Roshen, "Fringing field formulas and winding loss due to an air gap," in *IEEE Trans. Magn.*, vol. 43, no. 8, pp. 3387–3394, Aug. 2007.

[30] J. Hu and C. R. Sullivan, "AC resistance of planar power inductors and the quasidistributed gap technique," in *IEEE Trans. on Power Electron.*, vol. 16, no. 4, pp. 558-567, July 2001.

[31] "3F36 - Material specification," Ferroxcube, June 2013. [Online]. Available: https://www.ferroxcube.com/upload/media/product/file/MDS/3f36.pdf

[32] M. D'Antonio, S. Chakraborty and A. Khaligh, "Improved Frequency-Domain Steady-State Modeling of the Dual-Active-Bridge Converter Considering Finite ZVS Transition Time Effects," in *IEEE Trans. on Power Electron.*, doi: 10.1109/TPEL.2020.3040708.

Michael D'Antonio (S'18) received the B.S. degree in electrical engineering in 2016 from the University of Maryland, College Park, MD, USA, where he is currently working toward the Ph.D. degree in electrical engineering.

His current research interests include the modeling, design, and optimization of high-efficiency and high power-density power electronic converter solutions for renewable energy, transportation electrification, and data center applications.

Shiladri Chakraborty (M'18) received the B.E. degree from Jadavpur University, Kolkata, India in 2008, the M.Tech. degree from the Indian Institute of Technology (IIT) Kanpur, India in 2012, and the Ph.D. degree from IIT Kharagpur, India in 2019, all in electrical engineering.

He is currently a Postdoctoral Associate at the University of Maryland, College Park, MD, USA. His research interests include dual-active-bridge converters, wide-band-gap semiconductor-based converters, integrated packaging of power switches and high-frequency magnetics.

Alireza Khaligh (S'04, M'06, SM'09) is a Professor and the Director of Maryland Power Electronics Laboratory at the Department of Electrical and Computer Engineering (ECE) and the Institute for Systems Research (ISR), University of Maryland, College Park, MD, USA. He has authored or coauthored more than 200 journal and conference papers. His major research interests include modeling, analysis, design, and control of power electronic converters for transportation electrification, renewable energies, Internet of Things, and wearable electronics.

Dr. Khaligh is the Deputy Editor-in-Chief for the IEEE TRANSACTIONS on TRANSPORTATION ELECTRIFICATION.